Proximity-enhanced valley Zeeman splitting at the WS$_2$/graphene interface

To cite this article: Paulo E Faria Junior *et al* 2023 *2D Mater.* **10** 034002

View the article online for updates and enhancements.

2D Materials

PAPER

Proximity-enhanced valley Zeeman splitting at the WS$_2$/graphene interface

Paulo E Faria Junior[1],[*] ⓘ, Thomas Naimer[1] ⓘ, Kathleen M McCreary[2] ⓘ, Berend T Jonker[2], Jonathan J Finley[3], Scott A Crooker[4] ⓘ, Jaroslav Fabian[1] ⓘ and Andreas V Stier[3],[4] ⓘ

[1] Institute for Theoretical Physics, University of Regensburg, 93040 Regensburg, Germany
[2] Materials Science and Technology Division, Naval Research Laboratory, Washington, Washington, DC 20375, United States of America
[3] Walter Schottky Institut and TUM School of Natural Science, Technische Universität München, Am Coulombwall 4, 85748 Garching, Germany
[4] National High Magnetic Field Laboratory, Los Alamos, NM 87545, United States of America
[*] Author to whom any correspondence should be addressed.

E-mail: Paulo-Eduardo.Faria-Junior@physik.uni-regensburg.de

Keywords: TMDs, graphene, valley Zeeman effect, proximity

Supplementary material for this article is available online

Abstract

The valley Zeeman physics of excitons in monolayer transition metal dichalcogenides provides valuable insight into the spin and orbital degrees of freedom inherent to these materials. Being atomically-thin materials, these degrees of freedom can be influenced by the presence of adjacent layers, due to proximity interactions that arise from wave function overlap across the 2D interface. Here, we report 60 T magnetoreflection spectroscopy of the A- and B- excitons in monolayer WS$_2$, systematically encapsulated in monolayer graphene. While the observed variations of the valley Zeeman effect for the A- exciton are qualitatively in accord with expectations from the bandgap reduction and modification of the exciton binding energy due to the graphene-induced dielectric screening, the valley Zeeman effect for the B- exciton behaves markedly different. We investigate prototypical WS$_2$/graphene stacks employing first-principles calculations and find that the lower conduction band of WS$_2$ at the K/K' valleys (the CB$^-$ band) is strongly influenced by the graphene layer on the orbital level. Specifically, our detailed microscopic analysis reveals that the conduction band at the Q point of WS$_2$ mediates the coupling between CB$^-$ and graphene due to resonant energy conditions and strong coupling to the Dirac cone. This leads to variations in the valley Zeeman physics of the B- exciton, consistent with the experimental observations. Our results therefore expand the consequences of proximity effects in multilayer semiconductor stacks, showing that wave function hybridization can be a multi-step energetically resonant process, with different bands mediating the interlayer interactions. Such effects can be further exploited to resonantly engineer the spin-valley degrees of freedom in van der Waals and moiré heterostructures.

1. Introduction

Van der Waals layered materials allow for the assembly of intentionally designed stacks with a dedicated topology or functionality [1–6]. A key concept in this regard are proximity effects, where properties of a material or an ordered state are transferred from one layer to another without strongly affecting its electronic structure [7]. Nevertheless, a direct overlap of the wave functions in the adjacent layers is required

for the proximity effect to take place. For example, pristine graphene (Gr) is a gapless Dirac semimetal with a linear dispersion relation around the K/K' points and negligible spin–orbit coupling (SOC) [8] while proximity effects from adjacent materials may significantly tailor its properties to acquire a positive or negative mass [9], spin polarization and SOC [10–16] or superconductivity [17–20].

In recent years, the interface of Gr with a monolayer transition-metal dichalcogenide (ML TMD) has

received wide attention [9, 11–16, 21–29]. This system provides the appealing situation of creating a heterojunction between a material with strong SOC (the ML TMD) and long spin lifetimes (Gr). With respect to spin physics, particular interest was given to the topic of proximity induced SOC in Gr due to the strong SOC of the TMD [9, 11–16, 21–26]. Typically, proximity effects in the Gr community are theoretically modeled as a perturbation to the low energy model Hamiltonian of the Dirac cone [3], while keeping the wave functions unmodified (taken as purely p_z orbitals in Gr).

From the perspective of the optical properties of ML TMDs, engineering the dielectric environment with hexagonal boron nitride [30–35] or Gr [34, 36, 37], has been shown to be a very efficient path for tunable modification of the exciton binding energy (E_B) or sub nm lateral modulation of the TMD band gap (E_g) [36, 38]. This unprecedented degree of freedom provides novel functionality with respect to lateral heterojunctions, a technological feature which is very hard to realize in conventional semiconductor technology. In terms of conventional semiconductor spin physics, changes in the band gap are associated with strong modifications of the band g-factors, particularly in materials with strong SOC [39–41]. Therefore, it is expected that the ability to modify the band gap in the TMDs provides a path to tailor its exciton valley Zeeman effect. Recent state-of-the-art first principles calculations [42–45] have shown how to properly evaluate the orbital angular momentum contribution to the exciton valley Zeeman effect in ML TMDs, taking into account the Bloch functions of conduction and valence band electrons. Interestingly, the exciton g-factor depends only weakly on the band gap, while the band g-factors are indeed more sensitive to E_g [42], as expected from conventional III–V semiconductors within the **k.p** framework [41, 46]. While the valley Zeeman physics in intrinsic monolayers [42–45, 47–49] and hetero/homo-bilayers [42, 45, 50–55] is relatively well understood based on the recent *ab initio* developments, the influence of finite carrier density [56–62] (see also theoretical efforts in [63, 64]) or the evolution of the (in-plane) spin and orbital degrees of freedom in multilayered van der Waals heterostructures [65] still require further work.

In this study, we systematically investigate the dependence of the 1 s exciton valley Zeeman g-factor on van der Waals heterostructures of monolayer WS$_2$ with graphene. We performed circularly polarized magneto-reflection spectroscopy up to 60 T on large area films of ML WS$_2$ grown by chemical vapor deposition (CVD). The films were transferred either directly on SiO$_2$, or were single/double encapsulated with monolayer Gr. Clear valley splittings for the A- and B- excitons ($X^{A,B}$) are observed, providing measurements of the associated exciton g-factors

for each assembled structure. While the g-factor of the X^A varies smoothly and consistently with the band gap renormalization and size of the exciton wave function, surprisingly the g-factor of X^B varies more strongly in magnitude and distinctly non-monotonic. We explore the microscopic origin of this behavior with detailed first-principles calculations on several prototypical WS$_2$/Gr heterostructures with different stacking, shifts and twist angles. We show that the WS$_2$ conduction bands at the Q point mediate the interaction between the lower conduction band (CB$^-$) at the K point and the graphene Dirac cone, leading to distinct changes on the orbital degree of freedom of CB$^-$ and, consequently, on the B- exciton g-factor. This mediated coupling happens because of the energetic alignment of the conduction band Q and CB$^-$ at K, which is absent in Mo-based TMDs. Furthermore, our quantitative account of the dielectric screening effects of Gr to the exciton g-factors (reduction of the band gap and localization of exciton wave function) strengthens our picture that the non-monotonic variations in $g_A - g_B$ are indeed signatures of the complex interlayer hybridization between WS$_2$ and Gr. Our results therefore expand the concept of proximity effects, revealing that interlayer wave function hybridization of adjacent crystalline layers can happen at different levels (mediated by different energy bands), a concept that is crucial for understanding the spin-valley physics of van der Waals and moiré heterostructures.

2. Experimentally determined valley Zeeman effect in WS$_2$/graphene systems

We depict a schematic of the experiment and the investigated sample stacks in figure 1(a). Large-area monolayer films of WS$_2$ were grown by CVD on SiO$_2$/Si or graphene substrates [66–68]. The monolayer nature and high quality of these samples were confirmed by photoluminescence and Raman spectroscopy maps [69–71]. The as-grown monolayers were transferred from the growth substrate to a Si/SiO$_2$ substrate via standard wet transfer methods. For the doubly graphene encapsulated WS$_2$ layer, a top graphene layer was wet-transferred on the WS$_2$/graphene CVD film on the target substrate. Magneto-reflectance studies were performed at cryogenic temperatures ($T = 4$ K) in a capacitor-driven 65 T pulsed magnet at the National High Magnetic Field Laboratory in Los Alamos. Details about the experimental setup can be found in the supplemental note I [72] and in [30]. A total of three samples of each batch were investigated with two separate spots on each of the three samples. Data shown in this manuscript are typical for each batch and the reported error bars derive from averages of all experiments done on each batch.
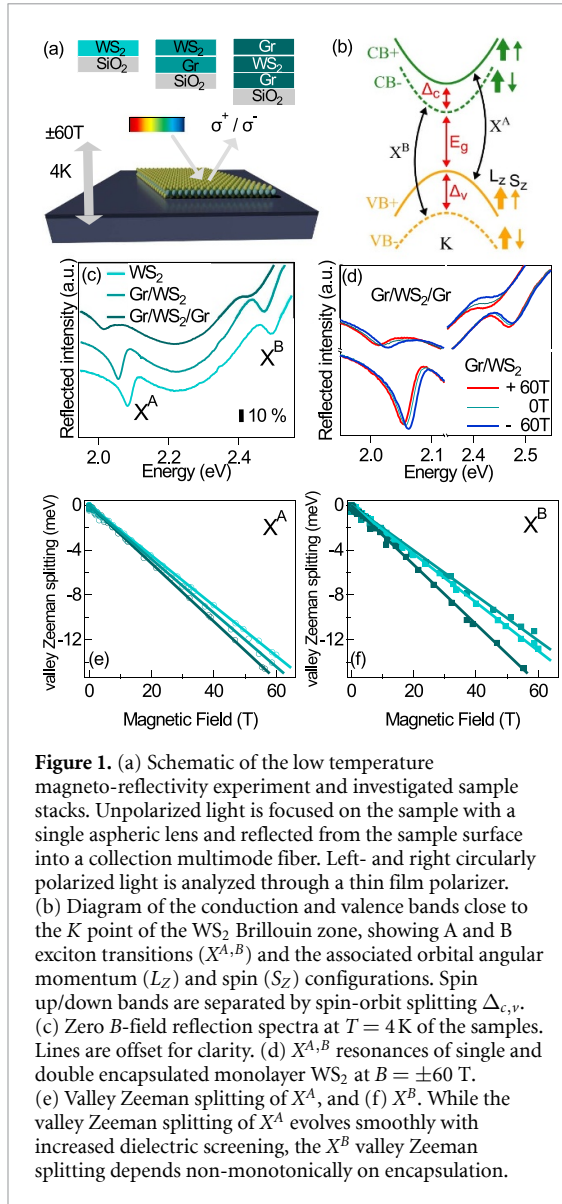
Figure 1. (a) Schematic of the low temperature magneto-reflectivity experiment and investigated sample stacks. Unpolarized light is focused on the sample with a single aspheric lens and reflected from the sample surface into a collection multimode fiber. Left- and right circularly polarized light is analyzed through a thin film polarizer. (b) Diagram of the conduction and valence bands close to the K point of the WS$_2$ Brillouin zone, showing A and B exciton transitions ($X^{A,B}$) and the associated orbital angular momentum (L_Z) and spin (S_Z) configurations. Spin up/down bands are separated by spin-orbit splitting $\Delta_{c,v}$. (c) Zero B-field reflection spectra at $T = 4$ K of the samples. Lines are offset for clarity. (d) $X^{A,B}$ resonances of single and double encapsulated monolayer WS$_2$ at $B = \pm 60$ T. (e) Valley Zeeman splitting of X^A, and (f) X^B. While the valley Zeeman splitting of X^A evolves smoothly with increased dielectric screening, the X^B valley Zeeman splitting depends non-monotonically on encapsulation.

We investigate the effect of graphene encapsulation on the exciton binding energy E_B and in particular the evolution of the valley Zeeman effect [73] of the A and B excitons, depicted in the single-particle energy diagram of the conduction and valence band in monolayer TMDs close to the K point of the Brillouin zone (BZ) (figure 1(b)). These excitons are observed as dips in the smooth reflection spectra depicted in figure 1(c) close to 2.05 eV (X^A) and 2.45 eV (X^B), respectively. No charged exciton features can be observed, confirming that the samples are close to charge-neutrality [74], although no active carrier control through gates has been employed here. As such, variations to the valley Zeeman effect due to resident carriers and the resulting Landau level physics can be excluded from our conclusions in the following analysis. The energy difference between X^A and X^B at zero magnetic field is given by the difference in the respective exciton binding energy and the SOC-induced splitting of the conduction (Δ_c) and valence band (Δ_v). As mentioned

in the introduction, graphene encapsulation successively introduces screening for the interband transitions in the TMD ML. This directly affects the band gap and E_B, causing the excitonic transitions to shift with varying encapsulation (see figure 1(c)). The effect of the increased screening on the 2D excitons can be probed in high field magnetospectroscopy.

In a magnetic field, the exciton energies shift following the relation

$$\Delta E_{A,B}(B) = \sigma_{A,B}B^2 + \frac{1}{2}\tau g_{A,B}\mu_B B, \qquad (1)$$

where the diamagnetic shift,

$$E_{\mathrm{dia}} = \sigma B^2 = e^2 \langle r^2 \rangle_{1s} B^2 / 8m_r, \qquad (2)$$

the reduced mass of the exciton is $m_r = (1/m_e + 1/m_h)^{-1}$ and the exciton ground state rms size is $(r_1 = \sqrt{\langle r^2 \rangle_{1s}})$. $\tau = \pm 1$ is the K/K' valley index, $\mu_B = e\hbar/2m_0$ is the Bohr magneton, and $g_{A,B}$ are the valley Zeeman g-factors of the excitons, related to the relevant energy bands by

$$g_A = 2\left[g_z(\mathrm{CB}^+, \mathrm{K}) - g_z(\mathrm{VB}^+, \mathrm{K}) \right]$$
$$g_B = 2\left[g_z(\mathrm{CB}^-, \mathrm{K}) - g_z(\mathrm{VB}^-, \mathrm{K}) \right] \qquad (3)$$

with $g_z(n, \vec{k})$ being the out-of-plane g-factor of the Bloch band n with wave vector $\vec{k}$ (see the relevant bands in figure 1(b)).

Figure 1(d) shows the reflection spectra of $X^{A,B}$ for the single and doubly Gr-encapsulated WS$_2$ at zero and the maximum ± 60 T applied magnetic field. A valley Zeeman splitting of ≈ 12 meV for each, $X^{A,B}$ resonance, analyzed in detail below, is observed. Both resonances shift to lower (higher) energy in positive (negative) fields, indicating a negative g-factor. The spectral features were fit using complex (absorptive and dispersive) Lorentzian lineshapes to extract the transition energy. Although the exact position of each resonance at zero magnetic field is difficult to determine precisely due to the smoothly varying background, the magnetic field dependent shifts can be exactly determined, as the background is unaffected during the magnetic field pulse. As such, the diamagnetic shift and the valley Zeeman splitting can be simply determined from the average and difference of the exciton B-dependent shift in positive and negative fields. In the supplemental note II–IV [72], we provide further details of the dielectric effects resulting in the decrease of the exciton binding energy. Figures 1(e) and (f) show the deduced valley Zeeman splittings for X^A and X^B, respectively. While the magnetic moment of the A-exciton smoothly increases in magnitude with increasing encapsulation, surprisingly, g_B evolves in a distinctly non-monotonic manner. This can be seen in the raw data of figure 1(f), where clearly the B-exciton of the double-encapsulated WS$_2$ splits significantly more than that of the single sided encapsulated TMD. The

Table 1. Experimentally determined g-factors from the linear fittings of figures 1(e)–(f). The experimental error is 0.1.

	WS_2	Gr/WS_2	$Gr/WS_2/Gr$
g_A	−3.8	−4.0	−4.2
g_B	−3.7	−3.3	−4.5
$g_A - g_B$	−0.1	−0.7	0.3

collected *g*-factor values are given in table 1. The unexpected behavior of the markedly different evolution of the exciton *g*-factors, best highlighted through the difference $g_A - g_B$, is the key experimental result of this study and can only be explained by taking interface hybridization of the wave functions into account.

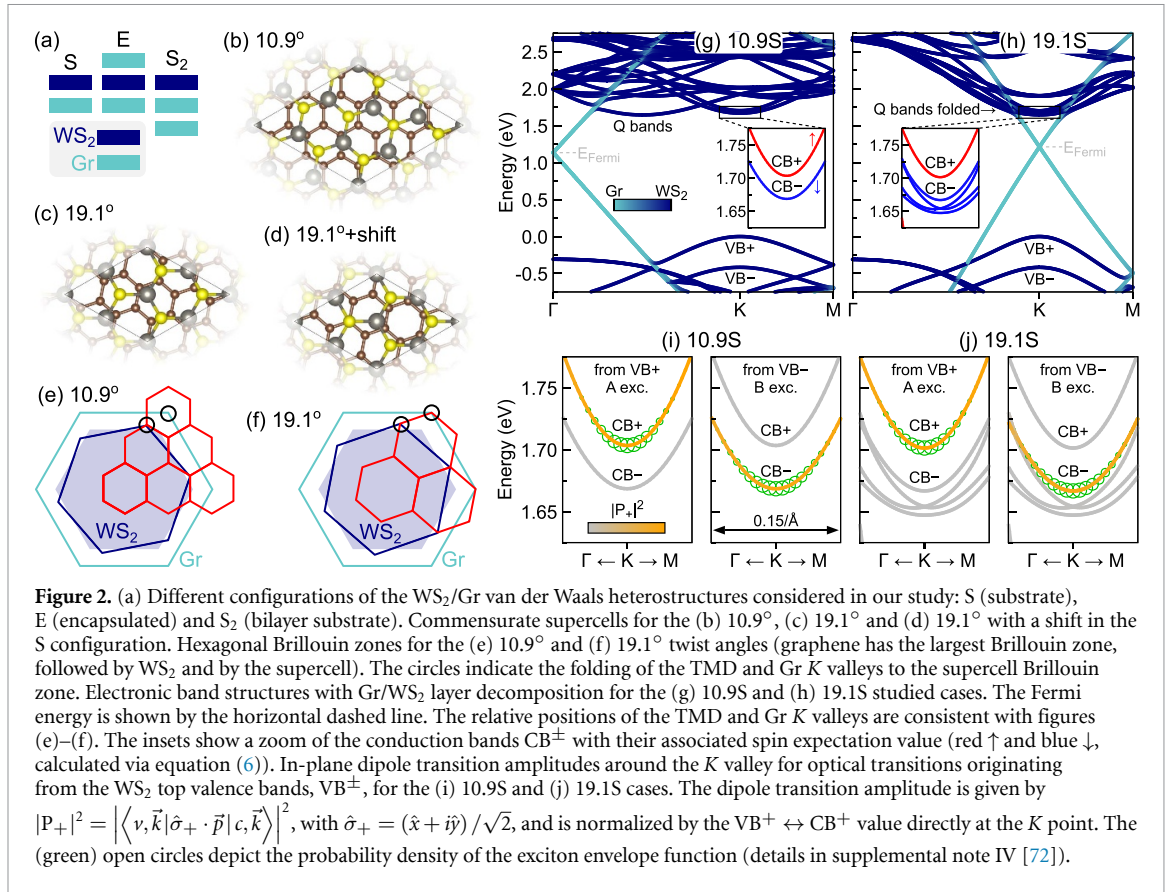## 3. Proximitized valley Zeeman physics in WS_2/graphene heterostructures

The interlayer hybridization of different layered materials is typically dependent on several parameters such as the lattice mismatch, the twist angle, the atomic registry, and so on. To investigate proximity effects in the valley Zeeman physics of WS_2/Gr van der Waals heterostructures, we consider several prototypical systems with different stackings and twist angles, calculated from first principles. The electronic properties are calculated via density functional theory (DFT) using the an all-electron full-potential implementation within WIEN2k [75], one of the most accurate DFT codes available [76], which has been successfully applied to investigate the microscopic nuances of SOC and spin-phenomena in 2D materials and their van der Waals heterostructures (including, but not limited to, Gr and TMDs) [11, 12, 49, 77–81]. The computational details can be found in the supplemental note V [72]. We note that previous DFT works on TMD and Gr systems have considered different commensurate structures, with different strain values and twist angles [11, 12, 24, 26, 82–84], and therefore there is no unique recipe on how to construct the van der Waals heterostructures of TMDs and Gr. An important point for our analysis is that only Gr is strained, so that the observed changes in the WS_2 *g*-factors arise solely from the interlayer coupling between the two materials. Strain effects in the *g*-factors of monolayer TMDs have already been investigated in [49], while strain effects in Gr are known to influence the Fermi velocity of the Dirac cone [85], leaving other features practically unaltered.

In figure 2(a), we depict the TMD/Gr systems considered here and contemplate three different cases: graphene as a substrate (S), graphene encapsulation (E) and bilayer graphene as a substrate (S_2). The S and E cases are chosen to mimic the Gr/WS_2 and the $Gr/WS_2/Gr$ experimental samples discussed in section 2. The S2 configuration has no experimental counterpart in this study, but it is a typical

structure considered by the Gr community as a platform for proximity-induced SOC effects [86–89]. In figures 2(b)–(d), we show the atomic structures of the WS_2/Gr supercells for the different twist angles considered in this study, i.e. 10.9° in figure 2(b), 19.1° in figure 2(c) and 19.1° with an in-plane shift in figure 2(d). The encapsulated systems have an additional graphene layer on top of the TMD while the bilayer graphene cases have a second graphene layer below, either with AB (Bernal) or AA stacking. Particularly, these two twist angles we consider here (10.9° and 19.1°) provide a relatively small number of atoms (see supplemental note V [72] for the details of all the considered heterostructures) and different folding of *k* points (see next paragraph). Most importantly, these two twist angles capture fundamental microscopic insights of the interlayer hybridization physics and act as benchmark cases for us to draw important conclusions about larger moiré supercells and other twist angles.

In the reciprocal space, the twist angle defines how different *k* points of the individual layers are mapped, or folded, to the reciprocal space of the supercell. The first BZ of Gr, WS_2 and the resulting supercell are shown in figures 2(e) and (f) for 10.9° and 19.1°, respectively. Importantly, the relative alignment of the *K* points in TMD and Gr happen at different positions for the two different angles, thus serving as the limiting cases for our analysis of the interlayer coupling effect. In realistic systems with long moiré lengths in real space (10 s of nm), many more BZs of the supercell would fit in the TMD and Gr BZs and therefore many more *k* points of the individual layers would be folded to a single *k* point of the supercell BZ.

The folding of the different *k* points, as well as the interactions between the layers, can be directly seen in the electronic properties (akin to electronic levels interacting via weak periodic potentials [90]). In figures 2(g) and (h) we show the layer-resolved band structures for 10.9S and 19.1S cases, respectively. It is evident that these two choices of twist angle provide different alignments between the low energy TMD bands and the Dirac cone, i.e. for 10.9° (19.1°) the TMD bands are located at the *K* point and the Dirac cone is located at the Γ (*K*) point, in agreement with the expectations from figures 2(e) and (f). Furthermore, besides the folding of *k* points, the interlayer coupling between WS_2 and Gr induces splittings to the energy bands, more visible in the regions where dark and bright blue regions overlap. The valence bands $VB^\pm$ are nicely isolated from the other bands, whereas the conduction bands $CB^\pm$ (indicated by the black rectangles, expanded as the inset) show a different behavior, particularly, the folding of the *Q* point conduction bands to the *K* point in the 19.1S case. We highlight the spin orientation of these folded *Q* bands in the inset and they exhibit the same spin direction as in the CB^-.

Figure 2. (a) Different configurations of the WS$_2$/Gr van der Waals heterostructures considered in our study: S (substrate), E (encapsulated) and S$_2$ (bilayer substrate). Commensurate supercells for the (b) 10.9°, (c) 19.1° and (d) 19.1° with a shift in the S configuration. Hexagonal Brillouin zones for the (e) 10.9° and (f) 19.1° twist angles (graphene has the largest Brillouin zone, followed by WS$_2$ and by the supercell). The circles indicate the folding of the TMD and Gr K valleys to the supercell Brillouin zone. Electronic band structures with Gr/WS$_2$ layer decomposition for the (g) 10.9S and (h) 19.1S studied cases. The Fermi energy is shown by the horizontal dashed line. The relative positions of the TMD and Gr K valleys are consistent with figures (e)–(f). The insets show a zoom of the conduction bands CB$^{\pm}$ with their associated spin expectation value (red ↑ and blue ↓, calculated via equation (6)). In-plane dipole transition amplitudes around the K valley for optical transitions originating from the WS$_2$ top valence bands, VB$^{\pm}$, for the (i) 10.9S and (j) 19.1S cases. The dipole transition amplitude is given by $|P_+|^2 = \left| \left\langle v, \vec{k} | \hat{\sigma}_+ \cdot \vec{p} | c, \vec{k} \right\rangle \right|^2$, with $\hat{\sigma}_+ = (\hat{x} + i\hat{y})/\sqrt{2}$, and is normalized by the VB$^+$ ↔ CB$^+$ value directly at the K point. The (green) open circles depict the probability density of the exciton envelope function (details in supplemental note IV [72]).

In figures 2(i) and (j) we focus on the energy scale of the conduction bands CB$^{\pm}$ that are contained in the insets in figures 2(g) and (h). The color code, from gray to orange, indicates the amplitude of the dipole transition from the VB$^{\pm}$ with σ_+ circularly polarized light, in order to identify the optical transitions that contribute to $X^{A,B}$. Our calculations show that the selection rules still hold in the heterostructure and, more importantly, that the Q point folded bands are optically inactive. The exciton spreading in k-space is also shown (using the calculated values of the Gr/WS$_2$ case, discussed in section II with details in supplemental note IV [72]) and reveals that only a small region around the K point is relevant, in line with robust GW and Bethe-Salpeter equation (BSE) calculations in bare monolayers [91]. Therefore, we can investigate the signatures of the WS$_2$/Gr hybridization by simply computing the g-factors of CB$^{\pm}$ and VB$^{\pm}$ directly at the K points of the heterostructure.

In order to investigate the modified valley Zeeman physics due to the microscopic effects of WS$_2$/Gr interlayer hybridization and its signature on the experimentally observed exciton g-factors (given in equation (3)), we must evaluate the Zeeman shift of the Bloch band (generally identified by the index n and crystal momentum $\vec{k}$):

$$E_{zs}(n, \vec{k}) = \left[L_z(n, \vec{k}) + S_z(n, \vec{k}) \right] \mu_B B$$
$$= g_z(n, \vec{k}) \mu_B B, \quad (4)$$

where B is the external magnetic field (in the out-of-plane direction, z, as in figure 1(a), and $L_z(n, \vec{k})$, $S_z(n, \vec{k})$ and $g_z(n, \vec{k})$ are the orbital angular momenta, spin angular momenta and g-factor of the Bloch band, respectively. The calculation of the orbital angular momentum in the out-of-plane direction, $L_z(n, \vec{k})$ for a Bloch state is obtained via the summation-over-bands approach [42–46, 49, 92]

$$L_z(n, \vec{k}) = \frac{1}{im_0} \sum_{m \neq n} \frac{P_x^{n,m,\vec{k}} P_y^{m,n,\vec{k}} - P_y^{n,m,\vec{k}} P_x^{m,n,\vec{k}}}{E(n, \vec{k}) - E(m, \vec{k})}, \quad (5)$$

in which $P_\alpha^{n,m,\vec{k}} = \left\langle n, \vec{k} | p_\alpha | m, \vec{k} \right\rangle$ ($\alpha = x, y, z$), with $\vec{p}$ being the momentum operator, and the spin angular momentum is calculated as

$$S_z(n, \vec{k}) = \left\langle n, \vec{k} | \hat{\sigma}_z | n, \vec{k} \right\rangle, \quad (6)$$

with σ_z the Pauli matrix acting on the spin-up and spin-down states of the spinorial Bloch state. We note that, because of time-reversal symmetry, the relation $O(n, -\vec{k}) = -O(n, \vec{k})$ holds for $O = L_z, S_z, g_z$. For further details on this theoretical approach applied to TMDs, we refer to [42–45, 49].

The calculated orbital and spin angular momenta of the CB$^{\pm}$ and VB$^{\pm}$ bands are shown in figures 3(a) and (b), respectively, for the investigated WS$_2$/Gr heterostructures. Our results reveal that L_z of CB$^-$, highlighted by the gray area in figure 3(a), is distinctly modified, either increasing or decreasing with
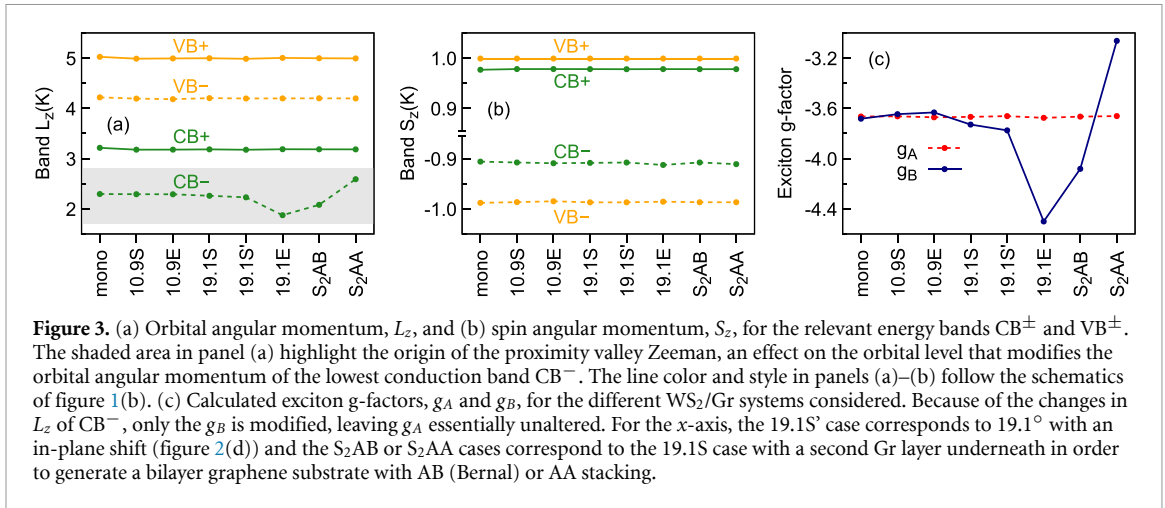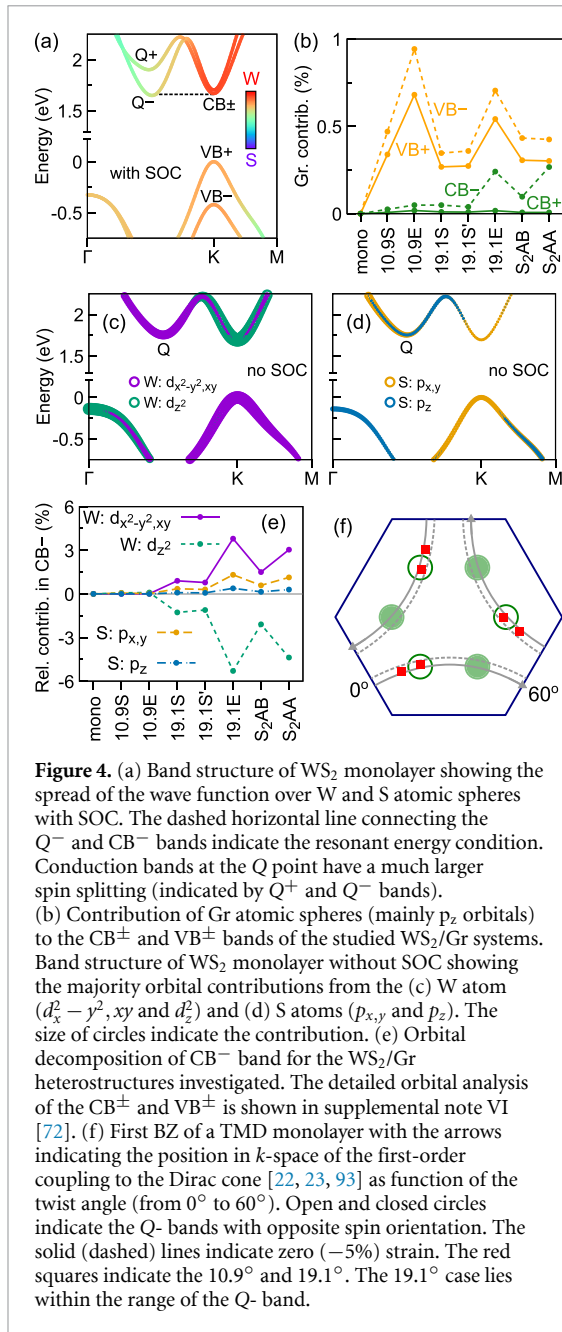
Figure 3. (a) Orbital angular momentum, L_z, and (b) spin angular momentum, S_z, for the relevant energy bands $CB^\pm$ and $VB^\pm$. The shaded area in panel (a) highlight the origin of the proximity valley Zeeman, an effect on the orbital level that modifies the orbital angular momentum of the lowest conduction band CB^-. The line color and style in panels (a)–(b) follow the schematics of figure 1(b). (c) Calculated exciton g-factors, g_A and g_B, for the different WS_2/Gr systems considered. Because of the changes in L_z of CB^-, only the g_B is modified, leaving g_A essentially unaltered. For the x-axis, the 19.1S' case corresponds to 19.1° with an in-plane shift (figure 2(d)) and the S_2AB or S_2AA cases correspond to the 19.1S case with a second Gr layer underneath in order to generate a bilayer graphene substrate with AB (Bernal) or AA stacking.

respect to the monolayer value depending on the particular system. The orbital angular momenta of the remaining bands ($VB^\pm$ and CB^+) barely changes. Additionally, we have not observed any changes in the spin angular momenta of the investigated bands. Combining the L_z and S_z of the energy bands, we can evaluate the A and B exciton g-factors via equation (3). The calculated values of g_A and g_B are shown in figure 3(c). While g_A is essentially constant, g_B is visibly changing (due to L_z of CB^-), revealing that there are indeed sizable contributions to the valley Zeeman of excitons arising from the interlayer coupling between WS_2 and Gr layers. Therefore, we attribute the experimentally observed changes of $g_A - g_B$ (table 1) to manifestations of the interlayer hybridization at the Gr/WS_2 interface. We note that the monolayer thickness is slightly modified when we perform the atomic relaxation of the heterostructure, but this effect is not responsible for the drastic changes in $g_A - g_B$ (see supplemental note V [72] for this comparison). Furthermore, we emphasize that our numerical calculations for L_z are fully converged with respect to the number of bands (see in supplemental note V [72] the comparison of monolayer and the 19.1E case).

At a first glance, it may seem counter intuitive that the largest change of the g-factor originates from the orbital degree of freedom of the *conduction* band CB^-. In figure 4(a) we show the wave function localization in the W and S atomic spheres for pristine WS_2 monolayer including SOC. The conduction bands, $CB^\pm$, at the K point are highly localized at the W atoms, while valence bands, $VB^\pm$, are more delocalized across the layer towards the S atoms. Since $VB^\pm$ bands are more delocalized, one might expect them to be more sensitive to the effect of the adjacent layers. In fact, the percentage of the wave function that 'leaks' to the Gr layer is larger for $VB^\pm$ bands, as shown in figure 4(b). Nevertheless, the largest changes to the band g-factors are observed for CB^-, as shown in figure 3(a). Interestingly, the spin degree of freedom

of CB^- band in W-based TMDs is also the most affected by strain [49].

We now turn to the central aspect of our theoretical analysis, i.e. the microscopic mechanism behind the changes in L_z of CB^-. For this purpose, we performed a detailed investigation of the orbital composition of the low energy bands $CB^\pm$ and $VB^\pm$. The monolayer WS_2 is summarized in figures 4(c) and (d) (SOC is neglected to simplify the visualization) and gives us the base values to compare with the investigated heterostructures. The conduction (valence) bands at the K point are dominated by d_{z^2} ($d_{x^2-y^2,xy}$) atomic orbitals of the W atom [73] while conduction bands at the Q point are mainly composed of $d_{x^2-y^2,xy}$ orbitals of the W atom. The p-like orbitals of the S atoms also provide a visible contribution, particular for the valence band at the K point and conduction bands at the Q point. In figure 4(e) we present the contribution of d-like (p-like) orbitals in W (S) atoms of the band CB^- for the different WS_2/Gr systems, considering the monolayer case as reference. Surprisingly, we observe a decrease of the d_{z^2} character of the W atom, accompanied with an increase of the $d_{x^2-y^2,xy}$ character of the W atom and p-like character ($p_{x,y}$ and p_z) of the S atoms, consistent with the orbital signature of the conduction band at the Q point. The full orbital decomposition analysis is shown in the supplemental note VI [72]. For the 19.1° cases, besides the folding of the Q bands to the K point, these Q bands also have a strong coupling to the Gr Dirac cone, as shown in figure 4(f) for the first-order Umklapp condition [22, 23, 93], thus mediating the coupling between CB^- and Gr states. A direct signature of such coupling between Q bands and the Gr Dirac cone is the drastic change of the orbital angular momentum of the folded Q bands, accompanied with increased contributions of the Gr atomic spheres (on the order of 1%–3%). These details are given in the supplemental note X [72]. Therefore, we can summarize the hybridization mechanism as following: the TMD conduction bands at the Q points (more
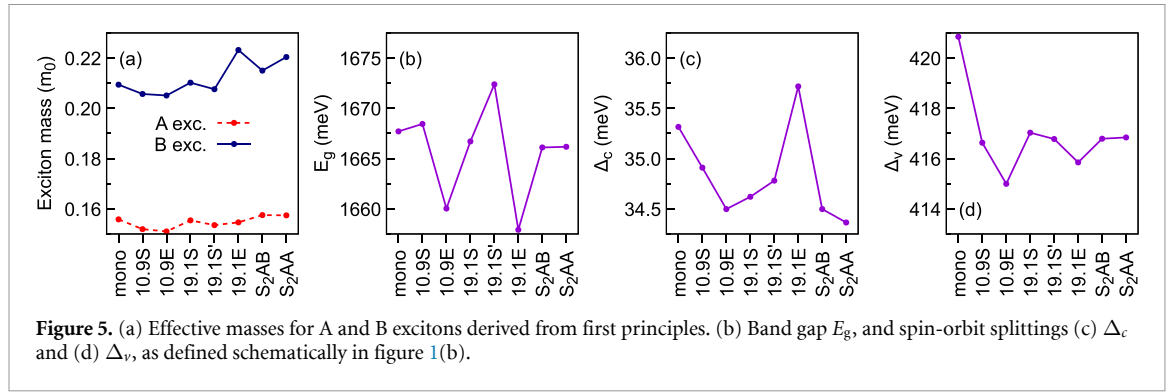
Figure 4. (a) Band structure of WS$_2$ monolayer showing the spread of the wave function over W and S atomic spheres with SOC. The dashed horizontal line connecting the Q^- and CB$^-$ bands indicate the resonant energy condition. Conduction bands at the Q point have a much larger spin splitting (indicated by Q^+ and Q^- bands). (b) Contribution of Gr atomic spheres (mainly p$_z$ orbitals) to the CB$^\pm$ and VB$^\pm$ bands of the studied WS$_2$/Gr systems. Band structure of WS$_2$ monolayer without SOC showing the majority orbital contributions from the (c) W atom ($d_x^2 - y^2, xy$ and d_z^2) and (d) S atoms ($p_{x,y}$ and p_z). The size of circles indicate the contribution. (e) Orbital decomposition of CB$^-$ band for the WS$_2$/Gr heterostructures investigated. The detailed orbital analysis of the CB$^\pm$ and VB$^\pm$ is shown in supplemental note VI [72]. (f) First BZ of a TMD monolayer with the arrows indicating the position in k-space of the first-order coupling to the Dirac cone [22, 23, 93] as function of the twist angle (from 0° to 60°). Open and closed circles indicate the Q- bands with opposite spin orientation. The solid (dashed) lines indicate zero (−5%) strain. The red squares indicate the 10.9° and 19.1°. The 19.1° case lies within the range of the Q- band.

depending on the particular geometry and stacking of the heterostructure.

We emphasize that the orbital angular momentum is not evaluated locally in the atomic spheres, but takes into account the whole spread of the wave function in the heterostructure, embedded in the transition matrix elements that enter the summation-over-bands expression of L_z in equation (5). The orbital decomposition analysis in figure 4 and supplemental note VI [72] provides a compact way of visualizing the spreading of the wave function throughout the system and which bands from the original Gr and TMD layer are hybridizing in the heterostructure. In terms of perturbative approaches and effective models, the orbital decomposition analysis extracted from DFT provides valuable microscopic insight on the type of perturbation order and coupling mechanism behind the observed effects (such as changes in L_z or S_z). For instance, a direct contribution of Gr states would encode some type of first order coupling, not necessarily leading to effective changes of the spin and/or orbital angular momenta (as in the case of the 10.9E system, which shows the largest contribution of Gr states to VB$^\pm$). On the other hand, the modification of the orbital decomposition within the TMD would encode higher order processes (virtual interlayer tunneling [23, 25]). It is beyond the scope of this study to provide a full account of this physical phenomena in terms of effective models, such as performed in [22, 23, 25], but, instead, reveal the underlying microscopic picture within DFT, similarly to [24, 26].

We have also analyzed the reduced exciton masses extracted directly from the DFT calculations, presented in figure 5(a), and found that the reduced mass for the A exciton barely changes while for the B exciton the reduced mass changes 0.005m_e, which are still rather weak to be clearly visible in experiments [33]. Moreover, we inspected the variations in the relevant energy scales E_g, Δ_c and Δ_v (defined in figure 1(b)). We found that the band gap varies by ∼15 meV, Δ_c varies ∼2 meV and Δ_v varies ∼6 meV for the different systems, which are relatively small changes. The associated correction to the g-factor due to variations in E_g is on the order of $\Delta E_g/E_g \approx 10^{-2}$, certainly smaller than the observed changes in figure 3. These small contributions originating from the energy parameters provide further support to our picture that changes in g_B are indeed manifestations of the complex nature of wave function hybridization across the different layers in the van der Waals heterostructure [4–6]. Finally, we note that effective masses and transition matrix elements are essentially unaffected over the different WS$_2$/Gr systems investigated (see figures 2(i) and (j) and figure 5(a)), providing further support to the perspective that Gr alters the exciton binding energies on

delocalized than K point bands) strongly couple with the Dirac cone in Gr (which host large g-factor values [94]) and then hybridize with the TMD conduction bands at the K point. Because of the nearly resonant condition (horizontal dashed line in figure 4(a)) and spin selectivity of folded Q bands and CB$^-$ bands (inset in figure 2(h)), the orbital angular momentum of CB$^-$ can be strongly altered and thus the valley Zeeman physics of the B exciton is more susceptible to changes. These unexpected proximity effects in the conduction bands of TMDs are also present in other van der Waals heterostructures. For instance, in TMDs coupled to ferromagnetic materials [95–99], the proximity-induced exchange splitting is also quite complex and can be stronger in the conduction band

Figure 5. (a) Effective masses for A and B excitons derived from first principles. (b) Band gap E_g, and spin-orbit splittings (c) Δ_c and (d) Δ_v, as defined schematically in figure 1(b).
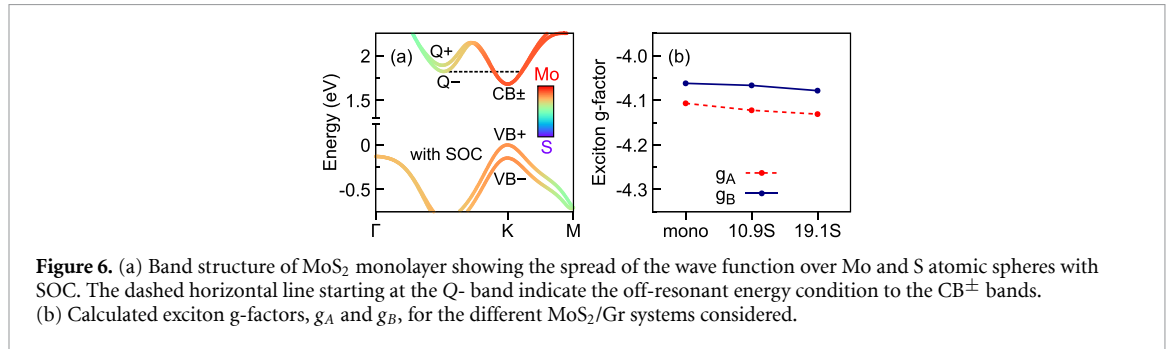
Figure 6. (a) Band structure of MoS_2 monolayer showing the spread of the wave function over Mo and S atomic spheres with SOC. The dashed horizontal line starting at the Q- band indicate the off-resonant energy condition to the $CB^{\pm}$ bands. (b) Calculated exciton g-factors, g_A and g_B, for the different MoS_2/Gr systems considered.

the dielectric level [34, 36, 100] (see also discussions in section 2 and supplemental note III [72]).

With this microscopic understanding, it would be interesting to consider a limiting scenario in which the modification of the valley Zeeman physics mediated by the Q point folded bands is essentially suppressed, thus isolating the direct contribution of Gr. Unlike monolayer WS_2, shown in figures 3(a)–(c), in Mo-based TMD monolayers the Q point conduction bands above the K valleys [101, 102] and therefore we expect this resonant coupling to be strongly suppressed in MoX_2/Gr (X = S,Se) systems. In order to verify this hypothesis and strengthen our understanding discussed above, we have analyzed the 10.9S and 19.1S cases for MoS_2/Gr heterostructures and summarize our findings in figure 6 (with further details given in supplemental note VIII [72]). Because the Q bands (either Q^- or Q^+) are energetically out-of-resonance with respect to the $CB^{\pm}$ bands (figure 6(a)), we found no significant changes to the exciton g-factors when comparing the monolayer with the 10.9S and 19.1S MoS_2/Gr heterostructures, shown in figure 6(b), in line with our understanding that Q point bands are crucial to mediate the interaction between Dirac cone of Gr and the K point bands of the TMD. We also note that the Q-folded bands of MoS_2 are drastically changed by the coupling with Gr Dirac electron (see supplemental note X [72]), but there is no energetic resonance to effectively transfer the orbital angular momentum to K-point bands.

4. Modified valley Zeeman physics by graphene as a dielectric

To complete our analysis, we investigate the modification of the valley Zeeman physics of WS_2 monolayer due to the influence of Gr on the dielectric level, motivated by the fact that the binding energy, E_B, and the exciton emission energy can be well explained in terms of dielectric screening effects [34, 36, 100] (see also section 2 and supplemental note III [72]). There are two relevant effects related to the influence of the dielectric screening on the exciton emission energy: (i) the band gap reduction (rigid band shift) [34, 103], which is $\sim$0.15(0.3) eV [36] in the Gr/WS_2 ($Gr/WS_2/Gr$) case; and (ii) the localization of the exciton wave function in k-space (increase of the exciton radius in real space), which can be directly extracted from our calculations (see table III in supplemental note IV [72] for the changes in the FWHM of the exciton envelope function). We note that recent experiments have shown that the measured band and exciton g-factors agree remarkably well with DFT calculations without excitonic corrections [104, 105]. However, it is in principle expected that excitonic effects renormalize the exciton g-factors by averaging the spin and orbital degrees of freedom around the K valleys [43, 106–110]. In order to provide a cohesive and comprehensive picture of the valley Zeeman physics, we explore the consequences of the band gap reduction and wave function localization by considering a pristine monolayer WS_2 (with a lat-

Table 2. Calculated exciton *g*-factors for pristine WS$_2$ monolayer within DFT for different values of scissor shifts to simulate the effect of band gap reduction.

	Scissor shift (eV)		
	0.0	−0.2	−0.4
g_A	−3.72	−3.77	−3.82
g_B	−3.74	−3.79	−3.85
$g_A - g_B$	0.02	0.02	0.03

tice parameter of 3.153 Å and thickness of 3.14 Å [101], without any relaxation from the heterostructure). The DFT calculations provide the fundamental information for the *g*-factors and effective masses of the low-energy bands (see figure 1(b) for the relevant bands). The exciton wave functions are calculated within the effective Bethe-Salpeter equation in *k*-space using the DFT effective masses as input (details in supplemental note IV [72]). The computational details for the DFT calculations can be found in the supplemental note V [72].

The band gap reduction due to the increased dielectric screening can be taken into account, *á la* **k.p** method, by applying a scissor shift to the calculated DFT band gap, i.e. a negative rigid energy shift to all conduction bands. These shifts are then incorporated in the energy differences that appear in the expression for the orbital angular momentum in equation (5). In table 2, we present the calculated exciton *g*-factors for scissor shifts of 0, −0.2 and −0.4 eV. The *g*-factors g_A and g_B become ∼0.1 more negative as we decrease the band gap by −0.4 eV. On the other hand, the difference $g_A - g_B$ is rather small (∼10^{-2}) and barely changes with the applied scissor shift. Therefore, the reduced band gap due to increased dielectric screening in WS$_2$/Gr heterostructures is unlikely to drastically modify the quantity $g_A - g_B$. We point out that our calculated *g*-factors given in table 2 are in excellent agreement with the experimental values given table 1 for the WS$_2$ case, which is consistent with the previous reports comparing DFT-based calculations with experimentally determined band and exciton *g*-factors in WSe$_2$ [104] and WS$_2$ [105]. We point out that the scissor shift procedure we used here may not capture the complete physics behind the band gap renormalization. For instance, this approach excludes non-local effects of the screening potential and possible renormalization effects in the momentum matrix elements that are present in more refined GW calculations [45, 64].

The effect of the dielectric screening on the spatial extension of the exciton wave function and how it translates to the exciton *g*-factor can be investigated by the following relation [43, 108, 109]

$$g_X = 2 \int d\vec{k} \left[g_z(c, \vec{k}) - g_z(v, \vec{k}) \right] \left| F_{c,v}(\vec{k}) \right|^2 \quad (7)$$

in which *X* is the exciton state generated by the conduction band, *c*, and valence band, *v*, described by the envelope function $F_{c,v}(\vec{k})$, with wave vector $\vec{k}$ centered at the *K* valley. Since the 1 s exciton envelope function in our approximation has a radial symmetry, we also consider such dependence for the *g*-factors, as discussed in supplemental note IX [72]. We summarize our results in table 3. The absolute values of both g_A and g_B become less negative, providing a worse comparison with experiments (considering the WS$_2$ case as reference, shown in table 1), but consistent with the renormalization effects observed in previous theoretical works [43, 106]. More importantly, the difference $g_A - g_B$ remains quite small and barely changes with the increased dielectric confinement. Furthermore, the calculated values of g_A and g_B are consistent whether we use the DFT masses or the corrected values (increased by ∼13% to approach experimental values [35]). Interestingly, the calculated g-factor change from the WS$_2$ to the Gr/WS$_2$/Gr case is 0.25 (0.29) for the A (B) excitons, which is in line with the experimental value of 0.29 (0.33). Our analysis suggest that the observed changes in $g_A - g_B$ do not originate from the dielectric effect on the exciton wave function. Our calculations here strongly rely on the charge-neutral character of the samples, otherwise substrate screening effect in the presence of free carriers could have a stronger impact on the neutral exciton *g*-factors [64].

Besides the dielectric effects, it is also worth mentioning the possible role of strain that could be present in the WS$_2$/Gr heterostructures due to the growth process. Typically, the reminiscent strain from the fabrication procedure was be estimated to be on the order of ±0.5% [111, 112]. Furthermore, recent calculations [49] have shown that in monolayer TMDs, g_A and g_B do not deviate from each other unless there is a sizable amount of compressive strain > 2%, leading to $g_A - g_B > 0$, which is accompanied with a reduction of the magnitude in both g-factors, i.e. g_A and g_B become less negative. This level of strain is very unlikely to be present in our samples, as this would be easily noticeable in the exciton energy (shifts due to strain are typically on the order of 100 meV/%) [102, 113].

We wrap up our theoretical analysis by emphasizing that the calculated dielectric effects of band gap reduction and exciton wave function localization are able to explain the monotonic behavior of the observed *g*-factors (they become more negative as the dielectric confinement increases). On the other hand, the drastic changes observed in $g_A - g_B$ (from negative to positive) can only be explained by our first principles calculations (section 3) including the microscopic effect of the interlayer coupling between WS$_2$ and graphene, which ultimately translates to changes in g_B originating from the orbital degree of freedom of the lower conduction band CB$^-$.

Table 3. Calculated exciton *g*-factors for pristine WS$_2$ monolayer including the effects of the exciton wave function localization in *k*-space. The calculations with DFT effective masses and corrected (Corr.) masses ($\sim$13% increase to reach experimental values) are shown.

		WS$_2$	Gr/WS$_2$	Gr/WS$_2$/Gr
DFT mass	g_A	-3.21	-3.37	-3.46
	g_B	-3.15	-3.34	-3.44
	$g_A - g_B$	-0.06	-0.03	-0.02
Corr. mass	g_A	-3.13	-3.32	-3.42
	g_B	-3.06	-3.28	-3.39
	$g_A - g_B$	-0.07	-0.04	-0.03

5. Concluding remarks

In summary, we reveal signatures of proximity-enhanced valley Zeeman physics, detected through high field magneto optical spectroscopy on the A- and B-exciton of Gr-encapsulated ML WS$_2$. We investigate the markedly different evolution of the X^A and X^B *g*-factors through first principles calculations by exploring different prototypical scenarios of the twist angle, stacking, and material composition. We reveal that the proximity effect due to the Gr-encapsulation mainly appears in the lowest K-point CB of WS$_2$ (CB$^-$) due to the modification of the orbital angular momentum, while the spin angular momentum is nearly unaffected. We reveal a mechanism, where the hybridization of the CB Q-point with CB$^-$ is mediated by the Gr Dirac cone and enhanced through commensurate stacking and the energetic alignment of the conduction bands at the Q- and K-point. This is a multi-step hybridization process involving different bands mediating the interlayer interactions.

We expect that interlayer hybridization effects due to commensurate band-folding are general for van der Waals and moiré heterostructures, also affecting spin dynamics at such interfaces. Particularly, we show how sensitive the *g*-factor is to the detailed nuances of the wave function hybridization, ultimately translated to the orbital degree of freedom in a non-intuitive manner. We therefore expand the concept of proximity effects in these heterostructures and show how magneto-optical experiments combined with first principles calculations can be used as a tool to quantify wave function hybridization. Future work may exploit the possibility to resonantly tune the coupling across layers via external electric fields, long-range moiré scales and mechanical deformations.

Data availability statement

The data cannot be made publicly available upon publication because they are not available in a format that is sufficiently accessible or reusable by other researchers. The data that support the findings of this study are available upon reasonable request from the authors.

ORCID iDs

Paulo E Faria Junior ⓘ https://orcid.org/0000-0002-1161-2059
Thomas Naimer ⓘ https://orcid.org/0000-0002-0967-6459
Kathleen M McCreary ⓘ https://orcid.org/0000-0003-2737-585X
Scott A Crooker ⓘ https://orcid.org/0000-0001-7553-4718
Jaroslav Fabian ⓘ https://orcid.org/0000-0002-3009-4525
Andreas V Stier ⓘ https://orcid.org/0000-0002-5476-1919

References

[1] Geim A K and Grigorieva I V 2013 *Nature* **499** 419
[2] Song J C W and Gabor N M 2018 *Nat. Nanotechnol.* **13** 986
[3] Sierra J F, Fabian J, Kawakami R K, Roche S and Valenzuela S O 2021 *Nat. Nanotechnol.* **16** 856
[4] Slobodkin Y, Mazuz-Harpaz Y, Refaely-Abramson S, Gazit S, Steinberg H and Rapaport R 2020 *Phys. Rev. Lett.* **125** 255301
[5] Plankl M *et al* 2021 *Nat. Photon.* **15** 594
[6] Barré E *et al* 2022 *Science* **376** 406
[7] Žutić I, Matos-Abiague A, Scharf B, Dery H and Belashchenko K 2019 *Mater. Today* **22** 85
[8] Castro Neto A H, Guinea F, Peres N M R, Novoselov K S and Geim A K 2009 *Rev. Mod. Phys.* **81** 109
[9] Avsar A, Ochoa H, Guinea F, Özyilmaz B, van Wees B J and Vera-Marun I J 2020 *Rev. Mod. Phys.* **92** 021003

[10] Avsar A *et al* 2014 *Nat. Commun.* **5** 4875

[11] Gmitra M and Fabian J 2015 *Phys. Rev. B* **92** 155403

[12] Gmitra M, Kochan D, Högl P and Fabian J 2016 *Phys. Rev. B* **93** 155104

[13] Avsar A, Unuchek D, Liu J, Sanchez O L, Watanabe K, Taniguchi T, Ozyilmaz B and Kis A 2017 *ACS Nano* **11** 11678

[14] Luo Y K, Xu J, Zhu T, Wu G, McCormick E J, Zhan W, Neupane M R and Kawakami R K 2017 *Nano Lett.* **17** 3877

[15] Cummings A W, Garcia J H, Fabian J and Roche S 2017 *Phys. Rev. Lett.* **119** 206601

[16] Fülöp B *et al* 2021 *npj 2D Mater. Appl.* **5** 82

[17] Ojeda-Aristizabal C, Ferrier M, Guéron S and Bouchiat H 2009 *Phys. Rev. B* **79** 165436

[18] Natterer F D, Ha J, Baek H, Zhang D, Cullen W G, Zhitenev N B, Kuk Y and Stroscio J A 2016 *Phys. Rev. B* **93** 045406

[19] Burset P, Yeyati A L and Martín-Rodero A 2008 *Phys. Rev. B* **77** 205425

[20] Högl P, Frank T, Kochan D, Gmitra M and Fabian J 2020 *Phys. Rev. B* **101** 245441

[21] Frank T, Högl P, Gmitra M, Kochan D and Fabian J 2018 *Phys. Rev. Lett.* **120** 156402

[22] Li Y and Koshino M 2019 *Phys. Rev. B* **99** 075438

[23] David A, Rakyta P, Kormányos A and Burkard G 2019 *Phys. Rev. B* **100** 085412

[24] Naimer T, Zollner K, Gmitra M and Fabian J 2021 *Phys. Rev. B* **104** 195156

[25] Péterfalvi C G, David A, Rakyta P, Burkard G and Kormányos A 2022 *Phys. Rev. Res.* **4** L022049

[26] Pezo A, Zanolli Z, Wittemeier N, Ordejón P, Fazzio A, Roche S and Garcia J H 2021 *2D Mater.* **9** 015008

[27] Aeschlimann S *et al* 2020 *Sci. Adv.* **6** eaay0761

[28] Krause R, Aeschlimann S, Chávez-Cervantes M, Perea-Causin R, Brem S, Malic E, Forti S, Fabbri F, Coletti C and Gierz I 2021 *Phys. Rev. Lett.* **127** 276401

[29] Hofmann N *et al* 2023 arXiv:2303.11856

[30] Stier A V, McCreary K M, Jonker B T, Kono J and Crooker S A 2016 *J. Vac. Sci. Technol.* B **34** 04J102

[31] Wierzbowski J *et al* 2017 *Sci. Rep.* **7** 12383

[32] Cadiz F *et al* 2017 *Phys. Rev. X* **7** 021026

[33] Raja A *et al* 2019 *Nat. Nanotechnol.* **14** 832

[34] Waldecker L *et al* 2019 *Phys. Rev. Lett.* **123** 206403

[35] Goryca M *et al* 2019 *Nat. Commun.* **10** 4172

[36] Raja A *et al* 2017 *Nat. Commun.* **8** 15251

[37] Lorchat E, López L E P, Robert C, Lagarde D, Froehlicher G, Taniguchi T, Watanabe K, Marie X and Berciaud S 2020 *Nat. Nanotechnol.* **15** 283

[38] Tebbe D, Schütte M, Watanabe K, Taniguchi T, Stampfer C, Beschoten B and Waldecker L 2022 arXiv:2212.00118

[39] Enderlein R and Horing N J M 1997 *Fundamentals of Semiconductor Physics and Devices* (Singapore: World Scientific)

[40] Yu P Y and Cardona M 2001 *Fundamentals of Semiconductors: Physics and Materials Properties* (Berlin: Springer)

[41] Winkler R 2003 *Spin-Orbit Coupling Effects in Two-Dimensional Electron and Hole Systems* vol 191 (Berlin: Springer)

[42] Woźniak T, Faria Junior P E, Seifert G, Chaves A and Kunstmann J 2020 *Phys. Rev. B* **101** 235408

[43] Deilmann T, Krüger P and Rohlfing M 2020 *Phys. Rev. Lett.* **124** 226402

[44] Förste J, Tepliakov N V, Kruchinin S Y, Lindlau J, Funk V, Förg M, Watanabe K, Taniguchi T, Baimuratov A S and Högele A 2020 *Nat. Commun.* **11** 4539

[45] Xuan F and Quek S Y 2020 *Phys. Rev. Res.* **2** 033256

[46] Roth L M, Lax B and Zwerdling S 1959 *Phys. Rev.* **114** 90

[47] Covre F S *et al* 2022 *Nanoscale* **14** 5758

[48] Blundo E *et al* 2022 *Phys. Rev. Lett.* **129** 067402

[49] Faria Junior P E, Zollner K, Woźniak T, Kurpas M, Gmitra M and Fabian J 2022 *New J. Phys.* **24** 083004

[50] Gillen R 2021 *Phys. Status Solidi* b **258** 2000614

[51] Förg M, Baimuratov A S, Kruchinin S Y, Vovk I A, Scherzer J, Förste J, Funk V, Watanabe K, Taniguchi T and Högele A 2021 *Nat. Commun.* **12** 1656

[52] Heißenbüttel M-C, Deilmann T, Krüger P and Rohlfing M 2021 *Nano Lett.* **21** 5173

[53] Zhao S *et al* 2022 arXiv:2202.11139

[54] Kipczak Ł *et al* 2023 *2D Mater.* **10** 025014

[55] Faria Junior P E and Fabian J 2023 *Nanomaterials* **13** 1187

[56] Arora A, Schmidt R, Schneider R, Molas M R, Breslavetz I, Potemski M and Bratschitsch R 2016 *Nano Lett.* **16** 3624

[57] Roch J G, Froehlicher G, Leisgang N, Makk P, Watanabe K, Taniguchi T and Warburton R J 2019 *Nat. Nanotechnol.* **14** 432

[58] Roch J G, Miserev D, Froehlicher G, Leisgang N, Sponfeldner L, Watanabe K, Taniguchi T, Klinovaja J, Loss D and Warburton R J 2020 *Phys. Rev. Lett.* **124** 187602

[59] Klein J *et al* 2021 *Phys. Rev. Res.* **3** L022009

[60] Klein J *et al* 2022 *Phys. Rev. B* **105** L041302

[61] Grzeszczyk M, Olkowska-Pucko K, Nogajewski K, Watanabe K, Taniguchi T, Kossacki P, Babiński A and Molas M R 2021 *Nanoscale* **13** 18726

[62] Li W, Lu X, Wu J and Srivastava A 2021 *Nat. Nanotechnol.* **16** 148

[63] Janak J F 1969 *Phys. Rev.* **178** 1416

[64] Xuan F and Quek S Y 2021 *npj Comput. Mater.* **7** 198

[65] Raiber S, Faria Junior P E, Falter D, Feldl S, Marzena P, Watanabe K, Taniguchi T, Fabian J and Schüller C 2022 *Nat. Commun.* **13** 4997

[66] McCreary K M, Hanbicki A T, Robinson J T, Cobas E, Culbertson J C, Friedman A L, Jernigan G G and Jonker B T 2014 *Adv. Funct. Mater.* **24** 6449

[67] McCreary K M, Hanbicki A T, Jernigan G G, Culbertson J C and Jonker B T 2016 *Sci. Rep.* **6** 19159

[68] Paradisanos I *et al* 2020 *Appl. Phys. Lett.* **116** 203102

[69] McCreary K M, Hanbicki A T, Singh S, Kawakami R K, Jernigan G G, Ishigami M, Ng A, Brintlinger T H, Stroud R M and Jonker B T 2016 *Sci. Rep.* **6** 35154

[70] McCreary K M, Hanbicki A T, Sivaram S V and Jonker B T 2018 *APL Mater.* **6** 111106

[71] Stier A V, McCreary K M, Jonker B T, Kono J and Crooker S A 2016 *Nat. Commun.* **7** 10643

[72] See supplemental material at [link] for details on the (I) experimental setup, (II) dielectric screening in 2D materials stacks, (III) determining the exciton binding energy from high field diamagnetic shift, (IV) calculation of the exciton binding energies and wavefunctions, (V) details on the first-principles calculations, (VI) details on the orbital decomposition, (VII) effect of lattice relaxation, (VIII) the MoS$_2$/Gr systems considered, (IX) excitonic effects on g-factors, and (X) spin and orbital angular momenta for the Q bands.

[73] Xiao D, Liu G B, Feng W, Xu X and Yao W 2012 *Phys. Rev. Lett.* **108** 196802

[74] Chernikov A, van der Zande A M, Hill H M, Rigosi A F, Velauthapillai A, Hone J and Heinz T F 2015 *Phys. Rev. Lett.* **115** 126802

[75] Blaha P, Schwarz K, Tran F, Laskowski R, Madsen G K and Marks L D 2020 *J. Chem. Phys.* **152** 074101

[76] Lejaeghere K *et al* 2016 *Science* **351** aad3000

[77] Gmitra M, Konschuh S, Ertler C, Ambrosch-Draxl C and Fabian J 2009 *Phys. Rev. B* **80** 235431

[78] Konschuh S, Gmitra M and Fabian J 2010 *Phys. Rev. B* **82** 245412

[79] Kurpas M, Gmitra M and Fabian J 2016 *Phys. Rev. B* **94** 155423

[80] Kurpas M, Faria Junior P E, Gmitra M and Fabian J 2019 *Phys. Rev. B* **100** 125422

[81] Faria Junior P E, Kurpas M, Gmitra M and Fabian J 2019 *Phys. Rev. B* **100** 115203

[82] Ratha S, Simbeck A J, Late D J, Nayak S K and Rout C S 2014 *Appl. Phys. Lett.* **105** 243502

[83] Paradisanos I *et al* 2020 *Appl. Phys. Lett.* **116** 203102

[84] Yang C-H and Chang S-T 2022 *Photonics* **9** 387

[85] Choi S-M, Jhi S-H and Son Y-W 2010 *Phys. Rev.* B **81** 081407

[86] Gmitra M and Fabian J 2017 *Phys. Rev. Lett.* **119** 146401

[87] Lee Y *et al* 2020 *Phys. Rev. Lett.* **124** 126802

[88] Amann J, Völkl T, Rockinger T, Kochan D, Watanabe K, Taniguchi T, Fabian J, Weiss D and Eroms J 2022 *Phys. Rev.* B **105** 115425

[89] Zhang Y, Polski R, Thomson A, Lantagne-Hurtubise E, Lewandowski C, Zhou H, Watanabe K, Taniguchi T, Alicea J and Nadj-Perge S 2023 *Nature* **613** 268

[90] Ashcroft N W and Mermin N D 1976 *Solid State Physics* (Harcourt: Brooks Cole)

[91] Katznelson S *et al* 2022 *Mater. Horiz.* **9** 1089

[92] Chang M-C and Niu Q 1996 *Phys. Rev.* B **53** 7010

[93] Koshino M 2015 *New J. Phys.* **17** 015014

[94] Frank T and Fabian J 2020 *Phys. Rev.* B **102** 165416

[95] Zollner K, Faria Junior P E and Fabian J 2019 *Phys. Rev.* B **100** 085128

[96] Zollner K, Faria Junior P E and Fabian J 2020 *Phys. Rev.* B **101** 085112

[97] Ge M, Wang H, Wu J, Si C, Zhang J and Zhang S 2022 *npj Comput. Mater.* **8** 32

[98] Zollner K, Faria Junior P E and Fabian J 2023 *Phys. Rev.* B **107** 035112

[99] Choi J, Lane C, Zhu J X and Crooker S A 2022 *Nat. Mater.* (https://doi.org/10.1038/s41563-022-01424-w)

[100] Stier A V, Wilson N P, Clark G, Xu X and Crooker S A 2016 *Nano Lett.* **16** 7054

[101] Kormányos A, Burkard G, Gmitra M, Fabian J, Zólyomi V, Drummond N D and Fal'ko V 2015 *2D Mater.* **2** 022001

[102] Zollner K, Faria Junior P E and Fabian J 2019 *Phys. Rev.* B **100** 195126

[103] Cho Y and Berkelbach T C 2018 *Phys. Rev.* B **97** 041409

[104] Robert C *et al* 2021 *Phys. Rev. Lett.* **126** 067403

[105] Zinkiewicz M *et al* 2021 *Nano Lett.* **21** 2519

[106] Chen S-Y *et al* 2019 *Nano Lett.* **19** 2464

[107] Gillen R 2021 *Phys. Status Solidi* b **258** 2000614

[108] Heißenbüttel M-C, Deilmann T, Krüger P and Rohlfing M 2021 *Nano Lett.* **21** 5173

[109] Amit T, Hernangómez-Pérez D, Cohen G, Qiu D Y and Refaely-Abramson S 2022 *Phys. Rev.* B **106** L161407

[110] Hötger A *et al* 2022 arXiv:2205.10286

[111] Mennel L, Furchi M M, Wachter S, Paur M, Polyushkin D K and Mueller T 2018 *Nat. Commun.* **9** 516

[112] Darlington T P *et al* 2020 *Nat. Nanotechnol.* **15** 854

[113] Frisenda R, Drüppel M, Schmidt R, Michaelis de Vasconcellos S, Perez de Lara D, Bratschitsch R, Rohlfing M and Castellanos-Gomez A 2017 *npj 2D Mater. Appl.* **1** 10